Reflection of solar wind hydrogen from the lunar surface

H. O. Funsten,[1] F. Allegrini,[2,3] P. A. Bochsler,[4] S. A. Fuselier,[2] M. Gruntman,[5] K. Henderson,[1] P. H. Janzen,[6] R. E. Johnson,[7] B. A. Larsen,[1] D. J. Lawrence,[8] D. J. McComas,[2,3] E. Möbius,[1,4] D. B. Reisenfeld,[6] D. Rodríguez,[9] N. A. Schwadron,[4] and P. Wurz[9]

Received 24 October 2012; revised 18 January 2013; accepted 24 January 2013; published 25 February 2013.

[1] The solar wind continuously flows out from the Sun and directly interacts with the surfaces of dust and airless planetary bodies throughout the solar system. A significant fraction of solar wind ions reflect from an object's surface as energetic neutral atoms (ENAs). ENA emission from the Moon was first observed during commissioning of the Interstellar Boundary Explorer (IBEX) mission on 3 December 2008. We present the analysis of 10 additional IBEX observations of the Moon while it was illuminated by the solar wind. For the viewing geometry and energy range (> 250 eV) of the IBEX-Hi ENA imager, we find that the spectral shape of the ENA emission from the Moon is well-represented by a linearly decreasing flux with increasing energy. The fraction of the incident solar wind ions reflected as ENAs, which is the ENA albedo and defined quantitatively as the ENA reflection coefficient R_N, depends on the incident solar wind speed, ranging from ~0.2 for slow solar wind to ~0.08 for fast solar wind. The average energy per *incident* solar wind ion that is reflected to space is 30 eV for slow solar wind and 45 eV for fast solar wind. Once ionized, these ENAs can become pickup ions in the solar wind with a unique spectral signature that reaches $3v_{SW}$. These results apply beyond the solar system; the reflection process heats plasmas that have significant bulk flow relative to interstellar dust and cools plasmas having no net bulk flow relative to the dust.

Citation: Funsten, et al. (2013), Reflection of solar wind hydrogen from the lunar surface, *J. Geophys. Res. Planets*, *118*, 292–305, doi:10.1002/jgre.20055.

1. Introduction

[2] For a large part of the lunar orbit, the solar wind bombards the Moon's surface with ions, continuously depositing nearly 1 kg of H per minute. The solar wind flows at, on average, 440 km/s (~1 keV/amu) and is typically composed of 96% H^+, 4% He^{2+}, and a small fraction of heavy ions. This energy and mass input into the lunar surface can physically and chemically process the lunar regolith, and most of the incident ions were assumed to be implanted in regolith grains [*Pillinger*, 1979; *Lucey et al.*, 2006]. However, a significant fraction of this mass escapes the Moon in the form of sputtered regolith atoms [*Wehner et al.*, 1963; *Hapke*, 1986; *Elphic et al.*, 1991; *Johnson and Baragiola*, 1991] and reflected solar wind ions observed as energetic ions [*Saito et al.*, 2008].

[3] Recently, a considerable fraction of solar wind ions was discovered to reflect from the lunar surface as energetic neutral atoms (ENAs). *McComas et al.* [2009a] measured an ENA albedo (reflection probability of solar wind ions from the lunar surface) of ~0.1 and showed that the energy spectrum and flux of ENAs reflected from the Moon depend on the solar wind speed and flux. Subsequent measurements of the reflection probability have yielded ~0.2 [*Wieser et al.*, 2009], a general range of values spanning ~0.1–0.3 with an average value of 0.24 [*Futaana et al.*, 2012], and ~0.09 [*Rodríguez et al.*, 2012].

[4] Several studies have also derived energy distributions of solar wind protons reflected as ENAs. *Futaana et al.* [2012] found that a Maxwell-Boltzmann (M-B) distribution well-represented the ENA energy distribution, with the derived M-B temperature correlating with the solar wind speed. *Rodríguez et al.* [2012] found that the ENA flux was generally constant up to ~0.5 keV, above which the flux precipitously dropped. These measurements were made with the SARA instrument [*Barabash et al.*, 2009] on the Chandrayaan-1 mission and the IBEX-Lo imager [*Fuselier*

[1]Los Alamos National Laboratory, Los Alamos, New Mexico, USA.
[2]Southwest Research Institute, San Antonio, Texas, USA.
[3]University of Texas at San Antonio, Physics and Astronomy Department, San Antonio, Texas, USA.
[4]University of New Hampshire, Durham, New Hampshire, USA.
[5]University of Southern California, Los Angeles, California, USA.
[6]University of Montana, Missoula, Montana, USA.
[7]University of Virginia, Charlottesville, Virginia, USA.
[8]Applied Physics Laboratory, Johns Hopkins University, Laurel, Maryland, USA.
[9]University of Bern, Bern, Switzerland.

Corresponding author: H. O. Funsten, Los Alamos National Laboratory, Los Alamos, NM 87545, USA. (hfunsten@lanl.gov)

©2013. American Geophysical Union. All Rights Reserved.
2169-9097/13-0/10.1002/jgre.20055

source: https://doi.org/10.7892/boris.44366 | downloaded: 6.5.2023

et al., 2009] on the Interstellar Boundary Explorer (IBEX) mission, respectively, both of which utilize a similar ENA detection methodology that is well-suited for measurements up to a few hundred electronvolts.

[5] The generally flat ENA spectral shape up to several hundred electronvolts in both of these studies is important here because the measurements of this study span an energy range 0.25–6 keV, derived using the IBEX-Hi sensor [*Funsten et al*., 2009a], which was optimized to measure ENAs over this energy range. The first observations of ENA emission from the Moon [*McComas et al*., 2009a] were obtained during the first orbit of IBEX science operations, IBEX Orbit 8 (IBEX Orbits are sequentially numbered from its launch in October 2008).

[6] IBEX is a Sun-pointed spinning spacecraft with a highly elliptical, 7.5 day orbit around Earth, with apogee about 78% of the distance from the Earth to the Moon's orbit [*McComas et al*., 2009b]. In June 2011, starting with IBEX Orbit 128, IBEX was placed into a stable, lunar-synchronous (1/3 the period of the Moon) orbit [*McComas et al*., 2011] that raised both perigee and apogee. This new orbit was explicitly designed to keep IBEX as far from the Moon as possible to avoid lunar gravitational perturbations and resulting chaotic behavior of the IBEX orbit. Therefore, the IBEX lunar observations before this orbital change, which are described here, represent the closest and therefore highest quality observations of the Moon anticipated for the duration of the IBEX mission.

[7] The observations of this paper cover the 11 IBEX encounters of the Moon in the solar wind during IBEX's original orbit, before June 2011, in which statistically significant counts were obtained in at least two IBEX-Hi energy passbands. The solar wind conditions vary substantially over these observations, while the viewing geometry of the Moon by IBEX relative to the solar wind velocity vector varies little, effectively allowing a controlled experiment of ENA emission from the Moon. This study focuses on understanding ENA emission from the Moon at energies above the threshold of the lowest IBEX-Hi energy passband, i.e., > 250 eV.

2. IBEX Observations of the Moon

2.1. IBEX and its Viewing Geometry

[8] IBEX was designed to measure the faint ENA emission from the outer heliosphere to understand the interaction of our heliosphere with the local interstellar medium [*McComas et al*., 2009b]. At IBEX, the ENA flux from the Moon is highly dependent on the distance to the Moon, but can reach a magnitude similar to the ENA flux from heliospheric sources such as the ribbon of enhanced flux and the globally distributed flux [e.g., *McComas et al*., 2009c; *Schwadron et al*., 2009]. These heliospheric ENAs represent a background flux for measurement and analysis of lunar ENAs and are subtracted from the lunar measurement.

[9] The IBEX-Hi Energetic Neutral Atom Imager [*Funsten et al*., 2009a] is a single-pixel imager designed to detect H ENAs with a 6.5° full width at half maximum (FWHM) field-of-view (FOV). The pixel is oriented perpendicular to the spacecraft spin axis, and a 360° circular swath of counts is accumulated in sixty 6° angular bins over each spacecraft spin. For reference, a spin angle of 0° corresponds to ecliptic north. Measurements are acquired of the same circular swath throughout an entire IBEX orbit when IBEX is at an altitude of at least 15 R_E. The imager cycles through six energy passbands every 12 spins. Because the count rate of lunar ENAs can be comparable to the count rates of heliospheric ENAs and various backgrounds, data for this study are processed over statistically significant time intervals of 1.53 h.

[10] Figure 1 shows the general viewing geometry of the Moon by IBEX. The solar wind radially expands from the Sun with thermal speeds much less than its flow speed, thus impacting the lunar surface as a nearly monodirectional beam composed primarily of protons. Because (1) the circular swath viewed by IBEX over its orbit lies nearly perpendicular to its

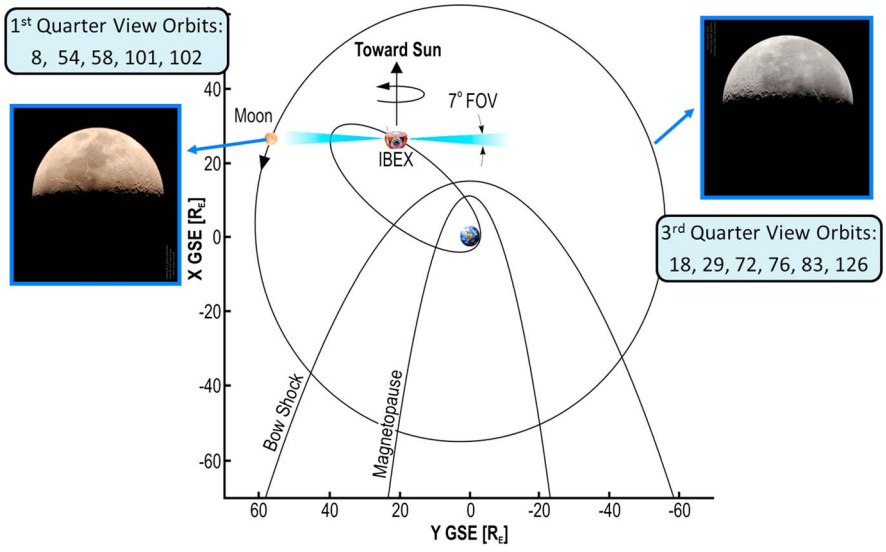

Figure 1. Because of its orbit and viewing geometry (a circular swath in a plane perpendicular to its Sun-pointed spin axis), IBEX observes a portion of the Moon illuminated by the solar wind that is nearly identical to the sunlit portions of the first or third quarter Moons.

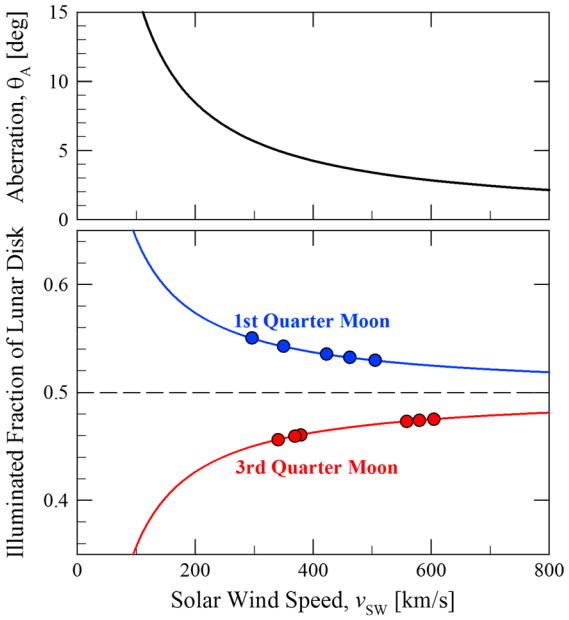

Figure 2. The speed (29.8 km/s) of the Earth-Moon system around the Sun introduces an angular aberration of the solar wind velocity vector as viewed at the Moon. The fraction of the Moon impacted by the solar wind as viewed by IBEX is therefore dependent on the solar wind speed. The points show the average solar wind speed for each of the IBEX observations of the Moon in this study.

Sun-pointed spin axis and (2) the solar wind flows, on average, radially outward from the Sun, IBEX views the Moon from two perspectives, similar to the first and third quarter of the sunlit Moon. The speed of the Earth-Moon system around the Sun ($v_{E\text{-}M}$ = 29.78 km/s) is perpendicular to the radial direction of the solar wind and causes a slight angular aberration of the solar wind at the Moon, resulting in solar wind illumination of slightly more than one fourth of the first quarter Moon and slightly less than one fourth of the third quarter Moon as viewed by IBEX. The aberration angle assuming a radial solar wind flow is

$$\theta_A = \tan^{-1}\left(v_{EM}/v_{SW}\right), \quad (1)$$

where v_{SW} is the solar wind speed. The area of the lunar disk illuminated by the solar wind as viewed by IBEX is therefore

$$A_I = 0.5\,\pi R_L^2[1 \pm \sin(\theta_A + \theta_{SA})], \quad (2)$$

where R_L = 1737 km is the average lunar radius and +/– corresponds to the first/third quarter viewing of the Moon by IBEX, respectively. The solar wind–illuminated area of the Moon also depends on the location of IBEX relative to the Moon, which was precisely derived for this study using the spacecraft ephemeris. Because the IBEX-Hi field-of-view over a spin is a narrow circle perpendicular to the IBEX spin axis, this effect can also be approximated by the angle θ_{SA} between the IBEX spin axis and the subsolar point in the ecliptic plane, which changes ~1° per day throughout an IBEX orbit. A positive (negative) value of θ_{SA} corresponds to early (late) in an orbit when the spin axis points beyond the west (east) limb of the Sun and views comparatively more (less) of the Moon that is illuminated by the solar wind. Note that this effect is only used to derive the ENA brightness from the location of IBEX; the convolution of the illuminated region of the Moon with the IBEX-Hi angular response (in equation (3)) is independent of this ENA source strength.

[11] Figure 2 shows the magnitude of this aberration as a function of the solar wind speed for both the first and third quarter viewing geometries. Also shown are the average solar wind speeds for the IBEX observations of this study, assuming purely radial flow of the solar wind and the IBEX spin axis points to the center of the Sun (θ_{SA} = 0). The difference in fractional illumination by the solar wind between the first and third quarters can be substantial; for example, the illuminated areas for the first quarter (IBEX Orbit 8) and third quarter (IBEX Orbit 18) events with the slowest average solar wind speeds vary by 20%.

[12] The Moon and IBEX are two bodies orbiting a central mass, Earth. Therefore, the Moon can trace a complex path through IBEX FOV, exacerbated by the highly elliptical IBEX orbit. Figure 3 shows the viewing geometry for IBEX Orbit 83, in which the Moon's location in the IBEX-Hi FOV and distance d_{LOS} to IBEX change nonlinearly with time. Knowledge of the IBEX location relative to the Moon and of the IBEX spin axis vector are important factors for quantitative derivation of the ENA albedo.

2.2. Energetic Neutral Atoms Flux Measurements

[13] Energetic neutral atoms from the Moon were observed in the lowest five of the six overlapping energy passbands in the IBEX-Hi energetic neutral atom imager [*Funsten et al.*, 2009a], at nominal energies E_C of 0.45, 0.71, 1.11, 1.74, and 2.73 keV with energy resolution $\Delta E_{FWHM}/E_C$ ranging from 0.47 at 0.45 keV to 0.65 at 2.73 keV (ΔE_{FWHM} is the full width at half maximum response at E_C). The lunar observations are based on the "qualified" triple coincidence counts that are the foundation of all published IBEX sky maps of the heliosphere [*McComas et al.*, 2012]. However, the specific data used for this study in which the Moon was near or in the IBEX FOV have been removed from the heliospheric sky maps because ENAs from the Moon represent a background for heliospheric ENA imaging.

[14] For the IBEX observation conditions, the Moon represents nearly a point source in the IBEX FOV, with a maximum full disc diameter of ~2.1° as viewed from IBEX at its closest viewing distance of 55 lunar radii (R_L), which occurred during IBEX Orbit 126. Because the IBEX angular response is 13° FWFM, ENAs of lunar origin can therefore fall into three 6° bins at most: the angular bin that coincides with the center of the Moon and the two adjacent angular bins. Complete spin-angle histograms are accumulated and reported every ~12 min. Because the lunar ENA flux can be comparable to the underlying heliospheric flux (e.g., when the lunar ENA flux overlaps the ribbon ENA flux [*Funsten et al.*, 2009b]), the lunar observations use coarser time bins of 1.53 h. This time interval is sufficiently long to provide statistically significant results and short enough to minimize variability of the solar wind parameters and of the IBEX viewing geometry.

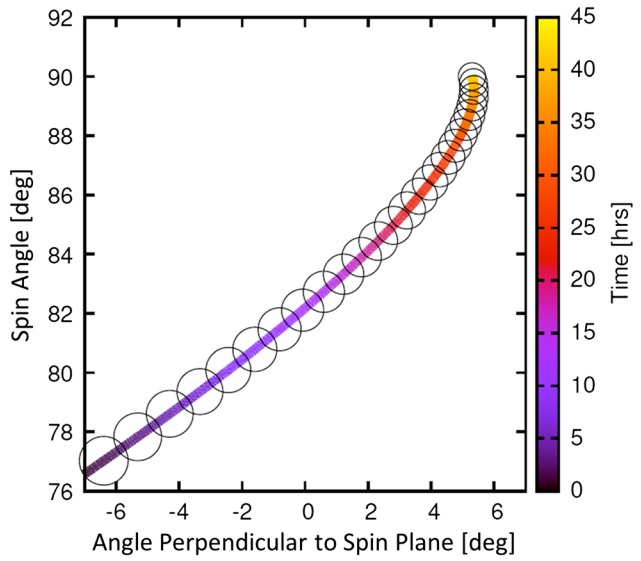

Figure 3. The transit of the Moon as viewed at IBEX throughout the encounter of IBEX Orbit 83. The spin angle is the angle of the circular swath observed by IBEX each spin throughout an IBEX orbit; a spin angle of 0° corresponds to ecliptic north. The single pixel FOV of IBEX-Hi has an angular resolution 13° full width at full maximum (FWFM), which is the extent of the horizontal axis (angle perpendicular to the spin plane). The circles qualitatively represent the angular size of the lunar disk at IBEX at regular 1.53 h intervals throughout the ~45 h encounter, over which statistically significant counts were obtained for ~25 h. The IBEX-Moon geometry can be complex and variable, but it is accurately determined using knowledge of the IBEX location and spin axis vector.

[15] The ENA flux from the Moon is superimposed on the ENA flux from the outer heliosphere as well as background counts from, e.g., penetrating radiation and magnetospheric plasma [*Wurz et al.*, 2009; *McComas et al.*, 2012]. Figure 4 shows an example of the raw data of the lunar observation during IBEX Orbit 83, which occurred in early June 2010. The four histograms show the "qualified" triple coincidence counts as a function of time and spin angle for each energy passband of IBEX-Hi. The plot to the right of each histogram shows the total number of counts over the entire observation period of each histogram. The peak of counts at the location of the Moon near 90° spin angle is clearly observed above the background distribution, particularly in the 0.71, 1.11, and 1.74 keV passbands. The solar wind during this encounter had an average speed 605 km/s (corresponding to an energy of ~1.8 keV for protons), and ENAs are clearly observed up to the 1.85 keV passband.

[16] Energetic neutral atoms from the Moon can be observed in a maximum of three 6° spin bins at the same time. The IBEX measurements at each energy passband *i* include ENAs from the Moon as well as heliospheric ENAs, which can vary significantly with spin angle in the vicinity of the ribbon; background from ambient magnetosheath or solar wind plasma, which typically changes slowly over spin angle; and noise (such as from cosmic rays) that is approximately constant over time and spin angle. First, we subtract the average heliospheric counts over the orbit at each spin angle; these are a routine data product that is used to construct the heliospheric ENA sky maps. Next, the known instrument backgrounds (from cosmic rays and solar wind sources) are subtracted using a semiempirical algorithm developed for generation of the heliospheric ENA sky maps

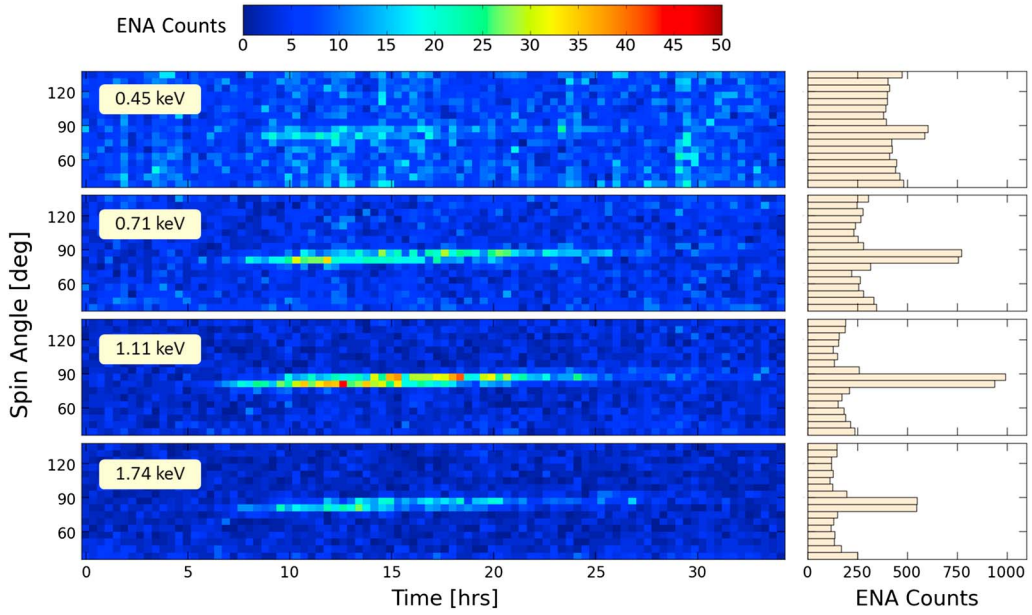

Figure 4. Lunar observation during IBEX Orbit 83 for the four lowest energy passbands of IBEX-Hi. Color histograms are the number of counts as a function of spin angle θ (binned to 6°) and time. Each time bin corresponds to 96 spins (~0.383 h) although quantitative analysis of the ENA counts is performed over time bins of 1.53 h for statistical significance. Spin angles of 0° and 180° correspond to ecliptic north and south, respectively. The plot to the right of each color histogram is the total number of counts for each spin bin acquired over the interval 6–27 h. The lunar signal lies near θ = 90° in all plots.

[*McComas et al.*, 2012]. Finally, the residual background is derived and subsequently subtracted by linear interpolation using the counts in the second and third 6° spin bin pixels located on either side of the two central pixels in which the Moon can register counts. The remaining lunar ENA counts C_0^i are obtained after integrating over time and the spin bins. For this paper, the statistical uncertainty associated with C_0^i includes the statistical uncertainty associated with the subtracted backgrounds.

[17] The solar wind speed v_{SW} and flux ϕ_{SW} were obtained from the Wind spacecraft [*Ogilvie et al.*, 1995] except for IBEX Orbit 58, in which Wind had a data dropout and measurements from the ACE spacecraft [*McComas et al.*, 1998] were used. Both spacecraft orbit the L1 point upstream of Earth. The time for the solar wind to propagate from L1 to the Moon was derived based on the measured solar wind speed, and the time of ENA propagation from the Moon to IBEX was calculated using the measured ENA energy and the distance from the Moon to IBEX. We note that the time of ENA propagation from the Moon to IBEX (~20 min for 0.25 keV H over a distance 100 R_L) is considerably smaller than the time of solar wind propagation from L1 to the Moon (~55 min for 1 keV H).

[18] Figure 5 summarizes the observations for each of the eleven orbits in which the Moon was immersed in the solar wind and was observed with statistically significant ENA counts by IBEX-Hi. The line-of-sight distance d_{LOS} from IBEX to the Moon ranged from 55 to 170 R_L and varied substantially during the lunar observations in IBEX Orbits 54, 76, 83, and 112. For the solar wind speed v_{SW} and flux ϕ_{SW}, the points represent the average and the bars represent the maximum and minimum values observed during an encounter. The total counts C_{TOT} represent the total counts for the entire lunar encounter at each energy passband. We note that, because of the significant width of the IBEX-Hi energy passbands, ENAs can be measured at nominal passband energies that are greater than the solar wind energy.

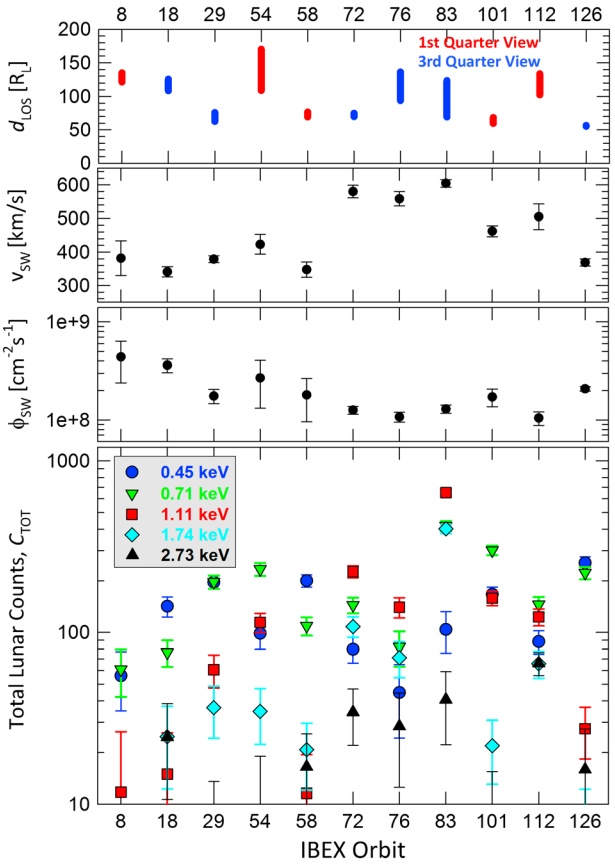

Figure 5. Summary of IBEX ENA observations of the Moon and the solar wind conditions during these observations. (top) Line-of-sight distance from IBEX to the Moon. (middle) Solar wind speed and flux measured by Wind spacecraft except for IBEX Orbit 58, which was measured by ACE spacecraft. (bottom) Total counts from lunar ENAs in each energy passband for each encounter.

3. Solar Wind Reflection from the Moon

[19] The solar wind impacts the lunar surface as a nearly monodirectional beam at a nearly constant energy-per-mass. Here, we only consider incident protons because they are the dominant species within the solar wind ions and because the IBEX-Hi ENA imager is most sensitive to H.

[20] Figure 6 shows the geometry of reflection from a small surface area. The surface normal is defined by the local surface flatness over a length scale similar to the depth that a reflected incident ion penetrates into regolith before it reflects (e.g., < 25 nm at 1 keV based on stopping and range of ions in matter (SRIM) calculations [*Ziegler et al.*, 2010] performed for this study), which is much less than the typical diameter of a lunar regolith grain of >50 μm [*McKay et al.*, 1991]. We define the angles α and β of the incident solar wind velocity $\vec{v}_{SW}$ and the exiting reflecting ENA velocity $\vec{v}_{ENA}$, respectively, relative to the surface normal. We define δ, which is the angle between $\vec{v}_{SW}$ and $\vec{v}_{ENA}$, as the phase angle. Importantly, because of the viewing geometry, IBEX measures only ENAs reflected at angles δ near 90°. ENAs emitted near the subsolar point (α ~ 0°) and detected at IBEX are reflected at β ~ 90°, whereas ENAs

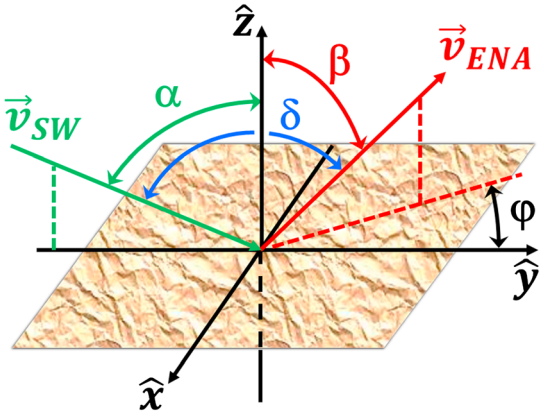

Figure 6. Geometry of scattering from the lunar surface. We define the phase angle δ as the angle between the incident solar wind and the direction of the reflected ENA. The local surface normal is *z*.

detected by IBEX that originate from the illuminated limb of the Moon (α ~ 90°) are emitted at β ~ 0°.

[21] Extensive research into plasma-wall interactions for fusion science and engineering have resulted in a rich

foundation of experimental data, theory, and models for light ion reflection from surfaces at energies similar to the solar wind [e.g., *Vicanek and Urbassek*, 1991; *Thomas et al*., 1992; *Eckstein*, 2010]. Of particular interest for magnetic confinement fusion is the reflection probability R_N of plasma ions and the fraction R_E of their incident energy retained after reflection from the wall of the confinement apparatus. For protons at normal incidence and incident energies 0.4, 1, and 2 keV on a solid with average mass 22 amu, we estimate from *Thomas et al.* [1992] R_N values of 0.31, 0.21, and 0.13 and R_E values of 0.15, 0.08, and 0.04, respectively, with most reflected particle emerging as neutral atoms [*Thomas et al*., 1992].

[22] The lunar surface is rough at scales ranging from the meter-to-kilometer range [*Rosenburg et al*., 2011] and, more importantly, is a regolith of grains of characteristic size of 10s to 100s of μm [*Carrier*, 2003] with porosity ~50% [*Houston et al*., 1974]. The latter has a substantial effect on optical reflection in which photons sample to depths of a number of grain diameters [*Shkuratov et al*., 2011]. The solar wind is therefore incident on the local, microscopic surface at myriad angles.

[23] Furthermore, shadowing introduced by large-scale and microscale roughness should substantially reduce the ENA albedo [*Bandurko et al*., 1990], similar to sputtering [*Cassidy and Johnson*, 2005]. However, in contrast to sputtering in which atoms are ejected at low energies and either stick to or are randomly reemitted from neighboring grains, ENAs have much higher energy and, therefore, a significant probability of a grazing reflection from an adjacent grain. Because of the complexity of the escape process, we ignore roughness in our model and simply note here that the probability of roughness-dependent escape of a sputtered particle is likely a lower bound for the escape of a reflected particle.

[24] The semiempirical SRIM Monte Carlo code [*Ziegler et al*., 2010] is routinely used to simulate the interaction of ions with solids. It does not account for surface roughness beyond the molecular level but can provide insight into the energy dependence and kinematics of the reflection process as well as upper limits to the ENA reflection coefficient R_N and energy reflection coefficient R_E. SRIM utilizes the binary collision approximation [*Sigmund*, 1982] in which an incident ion interacts independently with the target atoms prior to emerging as a reflected atom or ion. Because the penetrated layer of regolith grains have been made amorphous by the solar wind bombardment [*Keller and McKay*, 1993], this is particularly applicable for simulating the interaction of the solar wind with the lunar grains.

[25] The SRIM simulations are constructed using a monoenergetic, monodirectional beam of H^+ incident at a random angle with respect to the local surface normal, and the phase angle δ is calculated for each reflected atom. We have selected solar wind energies of 0.5, 1, and 2 keV to span the range of energies of the IBEX observations. We use an average composition of the fully illuminated Moon (the hemisphere covering the first and third quarter viewing), approximately 61% highlands and 39% mare composition based on a 10 wt % Fe abundance threshold for mare using global Fe abundance maps [*Lawrence et al*., 2002]. The highlands composition was derived from Apollo 16 landing site soil, and the mare composition represents the average compositions of Apollo 12 and Apollo 14 landing site soils [*Haskin and Warren*, 1991]. We consider only elements with at least 1% atomic abundance and use mass abundances of 45.8% O, 4.6% Mg, 12.0% Al, 21.6% Si, 9.3% Ca, and 6.6% Fe. Compared to the first quarter Moon, the third quarter Moon has 14 wt % more Mg, and 12 wt % less Al, 7 wt % less Ca, and 29 wt % more Fe. However, the dominant species O and Si, which comprise 79 wt %, together vary by less than 1%, so we expect that the compositional variation between first and third quarter views have minimal impact on the ENA albedo. We assume a density of 1.5 g/cm^3 [*Houston et al*., 1974].

[26] Figure 7 (top) shows the reflection probability of the entire Moon (per unit solid angle) as a function of the phase angle δ. Consistent with experimental results of light ion reflection from surfaces [*Thomas et al*., 1992; *Eckstein*, 2010] although in contrast to the results of *Futaana et al*. [2012], the simulations suggest that $R_N(\delta)$ decreases with increasing solar wind energy, likely because higher energy ions on average penetrate deeper before a hard collision so that the reflected ENA has lower probability of escape. For ENA emission from the entire Moon, the simulations yield values of 0.28, 0.23, and 0.19 for R_N and 0.12, 0.10, and 0.07 for R_E at energies 0.5, 1, and 2 keV, respectively. For comparison, the reflection (scaled to compare with the SRIM results) from a Lambertian sphere with an ideal diffusely reflecting surface illuminated by a beam of particles is also shown.

[27] These simulations of the Moon as a point source of emission suggest that the ENA flux per unit solid angle is greatest directly upstream of the Moon. As observed by *Schaufelberger et al*. [2011], the actual distribution of $R_N(\delta)$ is more strongly peaked toward the upstream direction, likely because ENAs reflected at small phase angles rarely encounter obstructions due to surface roughness, whereas surface roughness would suppress reflection at higher phase angles δ. This is analogous to the opposition effect in photometry that is attributed to surface roughness [*Buratti et al*., 1996; *Shkuratov et al*., 2011], a useful qualitative analog but not directly comparable because photons penetrate several grain diameters and follow different reflection kinetics. Nevertheless, precise observations an ENA opposition effect, which is not possible with the IBEX observations of this study, can provide critical insight into the lunar surface roughness at the scale sizes of individual grains.

[28] We note that the ENA flux from the Moon at large angles δ should be small. First, lab experiments show that atomic reflection from amorphous surfaces (such as the lunar regolith [*Keller and McKay*, 1993]) at grazing angles of incidence result in diffuse reflection rather than strong specular reflection [e.g., *Mayer et al*., 1995]. Thus, only diffuse scattering is expected for ENA emission near the solar wind terminator of the Moon. Second, an observer approaching a point downwind of the Moon, where $\alpha \rightarrow 90^\circ$ and $\delta \rightarrow 180^\circ$, sees a vanishingly small region illuminated by the solar wind, and thus a substantially reduced total ENA flux.

[29] The bottom panel of Figure 7 shows a normalized histogram of the energies of all reflected ENAs. A consistent shape is apparent for all solar wind energies, specifically that the distribution is generally flat at low energies and decreases approximately linearly with increasing energy above 300 eV up to the incident solar wind energy.

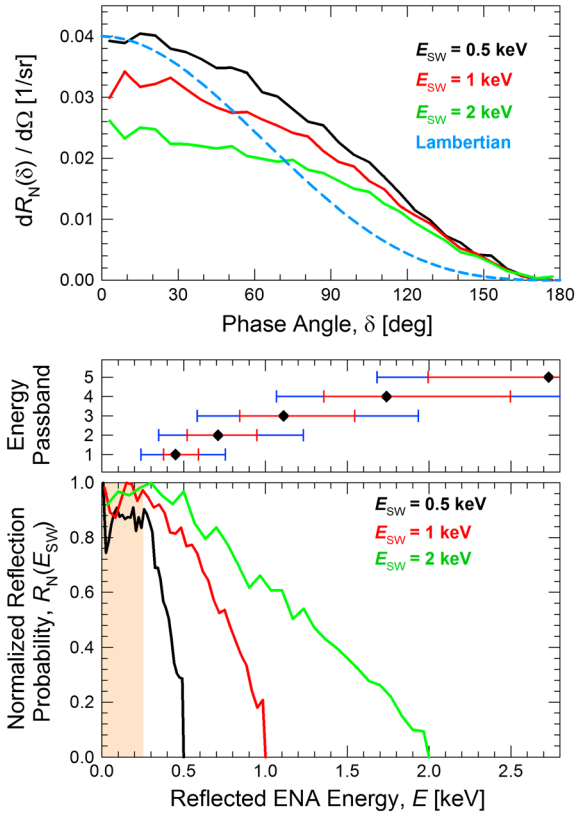

Figure 7. SRIM simulation for hemispherical illumination of the Moon. (top) Reflection probability (per unit solid angle) shows a systematic decrease over all phase angles with increasing solar wind energy. The reflected flux is strongly peaked in the upstream direction of the solar wind. (bottom) The SRIM-derived energy distribution of reflected ENAs. These spectral shapes of reflected ENAs are generally flat at energies below 0.3 keV; at higher energies the flux decreases nearly linearly with increasing ENA energy up to E_{SW} over the IBEX-Hi energy range. (middle) For comparison with the IBEX-Hi spectral sensitivity, the full width at half maximum response at each energy passband (red) as well as the full width at the 1% 1evel (blue) are shown. In the bottom panel, the tan stripe indicates the energy range below the ~250 eV threshold for detection by IBEX-Hi.

This shape is consistent with the empirical energy distribution of reflection of protons incident on carbon [*Aratari and Eckstein*, 1989].

4. Interpretation of Observations

[30] Because IBEX-Hi observes ENA emission over a limited number of overlapping energy passbands, we construct a forward model for the expected instrument count rates based on a lunar reflection function $R(E_{SW}, E, \delta, \theta)$. With this approach, we compare the count rate predicted by the forward model with the measured instrument count rate to assess the validity and derive the magnitude of the reflection coefficient $R_N(E_{SW})$, which is the reflection function integrated over all ENA energies and all emission angles from the Moon. The forward model propagates the solar wind flux ϕ_{SW} measured by Wind (or, by ACE for IBEX Orbit 58) to the Moon, applies the reflection function R at the solar wind energy and for the viewing (phase) angle δ between the aberrated solar wind direction and the IBEX-Moon vector, propagates the reflected flux from the Moon to IBEX, and convolves the modeled flux at IBEX with the IBEX-Hi energy geometric factor $G_i(E,\Omega)$ for each energy passband. The forward model predicts that a total of C_O^i lunar ENA counts per 1.53 h should be observed in each IBEX-Hi energy passband i:

$$C_O^i = \int_{FOV} \int_0^{E_{SW}} F_{ENA}(E_{SW}, E, \delta, \theta)\, G_i(E,\Omega) I(\Omega)\, dE\, d\Omega. \quad (3)$$

[31] Because the lunar disk diameter can subtend up to 2.1° during the closest IBEX observations (Orbit 126), we do not treat the Moon as a point source. Instead, we track the angular region $I(\Omega)$of the Moon illuminated by the solar wind as viewed from IBEX throughout the encounter and, for simplicity, we assume uniform ENA emission from this illuminated region. The IBEX-Hi geometric factor $G_i(E,\Omega)$ is separable into an energy-dependent response function for each energy passband i and an energy-independent point spread function $P(\Omega)$ based solely on the angular response of the collimator [*Funsten et al.*, 2009a]. We convolve $P(\Omega)$ with the illuminated region $I(\Omega)$ of the Moon as it traverses the IBEX field of view (e.g., Figure 3) for each 1.53 h observation of the Moon.

[32] The ENA flux as a function of ENA energy E at the entrance of the IBEX-Hi imager is

$$F_{ENA}(E_{SW}, E, \delta) = \phi_{SW}\, R(E_{SW}, E, \delta, \theta) \frac{A_I}{d_{LOS}^2}, \quad (4)$$

where A_I is obtained from equation (2), d_{LOS} is the distance from IBEX to the Moon, and θ is the azimuthal ENA emission angle around the aberrated solar wind velocity vector at subsolar point of the Moon, ranging from 0° to 360°.

4.1. Lunar Reflection Function

[33] The reflection function R is complicated because it represents multiple effects. At any location on the Moon, reflection depends on the microscopic regolith properties and surface orientation as well as the microscopic and macroscopic porosity and roughness that can trap a reflected ENA. These, in turn, depend on E_{SW}, E, and angles α, β, δ, and θ. Chandrayaan-1 ENA observations noted variation of reflected flux with these angles [*Schaufelberger et al.*, 2011] because it viewed a comparatively small spatial footprint of ENA emission from the Moon from a low altitude of 100–200 km.

[34] However, the Moon is sufficiently far from IBEX (the lunar disk as viewed by IBEX is <3°) that it can be treated in the reflection function as a point source of ENA emission. Furthermore, IBEX only views the Moon from two vantage points (first and third quarter Moon) over a limited range of phase angles δ near 90° at opposing azimuthal angles θ. Therefore, we construct $R(E_{SW}, E)$ for each observation as a function of only E_{SW} and E and uniformly distributed over δ and θ. This definition enables direct comparison of the model with IBEX data for δ near 90° and the first and third quarter vantage points. It is also straightforward to incorporate the functional dependence of R on δ and θ as needed.

[35] The results of the SRIM simulations (Figure 7, bottom panel) suggest that the energy dependence of the ENA flux should be, to first order, linear above the lowest energy detectable by IBEX-Hi (>250 eV). We also have empirical evidence of this linearity. For the lunar observation during IBEX Orbit 83 illustrated in Figure 4, IBEX was comparatively close to the Moon and the solar wind was fast, ranging from 580 km/s (1.75 keV) to 650 km/s (2.2 keV). This resulted in a copious ENA flux from the Moon that spanned five energy passbands. We apply the forward model for each energy passband independently by assuming a reflection coefficient R^i that is constant at each passband throughout the encounter, independent of ENA energy within the passband as well as variations of solar wind energy and flux. Therefore, for each energy passband we can extract R^i from $F_{ENA}(E_{SW}, E, \delta, \theta)$ in equation (4) and, also, the integrand of equation (3). Equation (3) simplifies to $C^i_O = R^i C^i_M$, where C^i_M is the output of the forward model assuming every incident solar wind ion backscatters from the lunar surface. The reflection coefficient at each energy passband i is thus derived using the ratio of the ENA counts C^i_O observed at IBEX to the counts C^i_M predicted by the forward model, i.e., $R^i = C^i_O/C^i_M$. The derived values of R^i, shown in Figure 8, follow a linear trend, and a linear fit to the data (weighted by the uncertainty of the observed counts) for the lowest four energy passbands yields $R^i = 0.17$–$0.080\ E$ [keV].

[36] The linear fit of the ENA flux reaches zero at 2.13 keV, which is close to both the average and maximum solar wind energies (1.5 h averaged) of 1.90 and 2.05 keV, respectively, for this encounter. Thus, the observed ENA emission results from reflected solar wind ions rather than a sputtering process, which is typically observed at much lower energies [*Eckstein*, 1997].

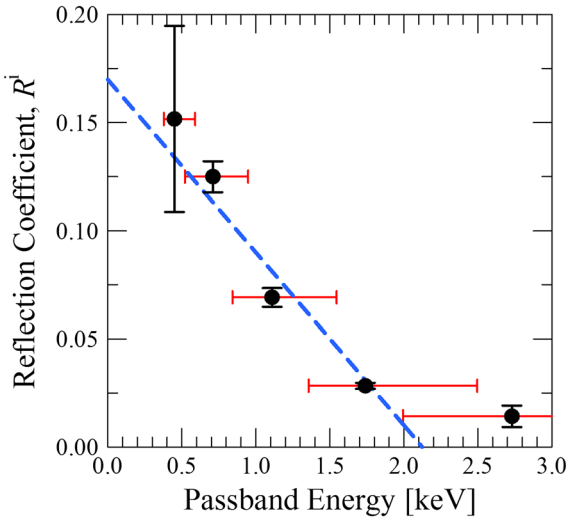

Figure 8. The derived reflection coefficient R^i at each energy passband i assuming that R^i is a constant, unique value for each individual energy passband throughout the lunar encounter. IBEX Orbit 83 had the brightest ENA emission as well as a high speed solar wind input with resulting ENAs that spanned all five energy passbands. R^i approximates the relative ENA flux across the energy passbands and demonstrates a linear spectral shape of ENAs emitted from the Moon over the IBEX-Hi energy range. The black vertical lines are the uncertainties in the measured counts. The red horizontal lines are the FWHM energy passband acceptance.

[37] The solar wind energy E_{SW} ideally represents the upper limit for the energy of a reflected ENA. Hydrogen ENAs with energies approaching E_{SW} result from Rutherford-type elastic scattering in which a light solar wind ion such as H^+ backscatters from a heavy regolith atom at or near the atomic surface of the regolith. For example, the maximum possible energy of H ENAs at a phase angle $\delta = 90°$ is 0.88 E_{SW} and 0.93 E_{SW} if backscattered from an O or Si surface regolith atom, respectively.

[38] Counts can appear in energy passbands at nominal energies higher than the average solar wind energy for two reasons. First, the solar wind properties are highly dynamic and contains populations with speeds quite different from the bulk speed. For example, the internal temperature can be high, the bulk speed can vary substantially over time, and the high speed wind often contains a secondary proton beam at a higher energy than the primary beam [*Feldman et al.*, 1993; *Hammond et al.*, 1995]. Second, the IBEX-Hi energy passbands are comparatively wide (FWHM energy resolution of $\Delta E/E$ ~70%), and ENAs with energy higher than the passband threshold but lower than the nominal passband energy can be measured. For example, in Figure 8 ENA counts from the Moon are observed in the nominal 2.7 keV energy passband even though the average solar wind energy for the encounter is 2.1 keV.

[39] For Figure 8 the utility of using a constant value of R^i for each energy passband and the accuracy of the linearity it reveals is based on a unique property of the convolution of a broad energy passband that is symmetric about its central energy with a linear spectral shape: the resulting measured flux is exactly equal to the actual flux at the central energy, independent of the slope of the linear spectrum. Therefore, in Figure 8 the linear spectral shape spanning the nearly symmetric IBEX-Hi energy passbands is internally consistent with the individual values derived for each passband that are independent of the slope of the linear spectrum. The exception, of course, is the 2.7 keV passband whose response function lies mostly above the average solar wind energy for the encounter. We note also that a small fraction of the nominal 1.74 keV passband of IBEX-Hi lies above E_{SW}.

[40] Because the IBEX measurements and the SRIM simulations both strongly indicate that the reflected ENA flux linearly decreases from ~250 eV to the solar wind energy, we construct the following reflection function:

$$R(E_{SW}, E) = \frac{R_N(E_{SW})}{2\pi E_{SW}}\left(1 - \frac{E}{E_{SW}}\right), \quad E \le E_{SW}, \tag{5}$$

where, as previously stated, we have assumed that $R(E_{SW}, E)$ is independent of phase angle δ and azimuth θ. Of course, the ENA energy E must always be less than E_{SW}, so $R = 0$ for $E > E_{SW}$. In this equation, the reflection coefficient $R_N(E_{SW})$ is the total reflection yield from the entire lunar surface uniformly distributed over 4π sr, i.e.,

$$R_N(E_{SW}) = \int_{4\pi\ \mathrm{sr}} \int_0^{E_{SW}} R(E_{SW}, E)\, dE\ d\Omega. \tag{6}$$

[41] The factor of 2π in equation (5) ensures that, upon integration of equation (6), a value of $R_N = 1$ corresponds to an albedo of unity, in which all incident solar wind protons are reflected from the lunar surface. Comparison of the linear model of equation (6) to the IBEX-Hi data relies on only a single fit parameter, R_N, at each solar wind energy.

4.2. ENA Albedo: The Reflection Coefficient, R_N

[42] The forward model using the linear reflection function was run with the evolving solar wind conditions and IBEX viewing geometry over the same time cadence (τ_{Hi} ~1.5) as the IBEX-Hi data acquisition. For each of the eleven encounters of the Moon in the solar wind, the modeled counts C_M^i, which assumes unity albedo, was scaled by the reflection coefficient R^i and compared with observed counts C_O^i for each time interval τ_{Hi} and each energy passband i, where $R^i = R_N(E_{SW}, E)$ with E equal to the value of the nominal passband energy. The single, energy-independent free parameter $R_N(E_{SW})$ in equation (5) was derived for each encounter for all energies combined using least squares fit to a straight line weighted by the uncertainty of observed counts. The results are shown in Figure 9 along with the derived value of $R_N(E_{SW})$ for each encounter.

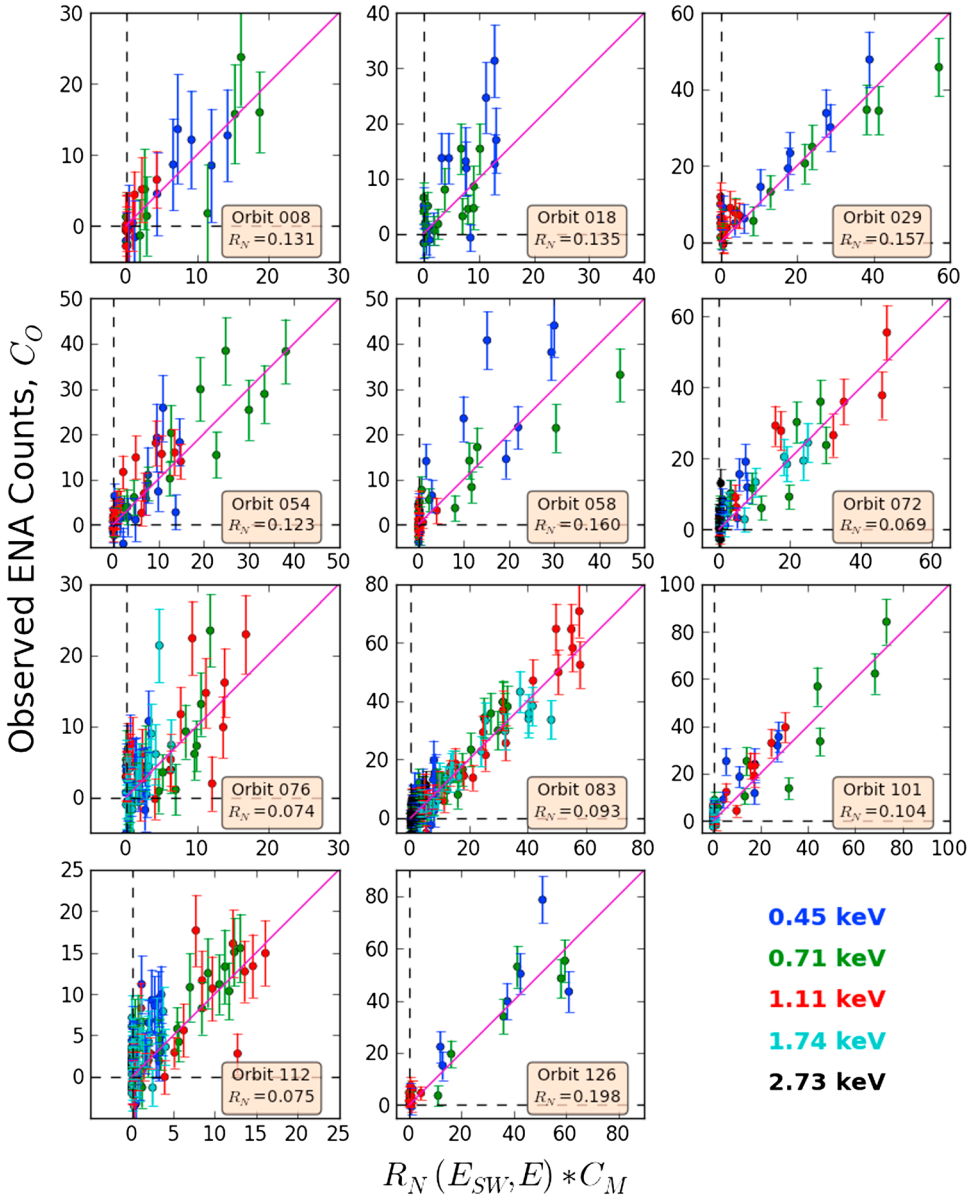

Figure 9. For each encounter of IBEX and the Moon, the observed ENA counts C_O per time interval τ_{Hi} ≈ 1.53 h at each IBEX-Hi energy passband is plotted as a function of the product of the modeled ENA counts C_M (which assumes an albedo of unity) and a reflection coefficient with an energy dependence represented by equation (5), which linearly decreases with increasing ENA energy. The error bars represent the Poisson counting statistics derived from the combination of ENA counts attributed to lunar origin and the ENA counts from nonlunar (i.e., background and heliospheric) origin. Ideal agreement between the model results and the observations would fall along the 45° magenta line.

[43] Ideal agreement between observations and model results when $C_O^i = R_N(E_{SW}, E)C_M^i$, which corresponds to the diagonal line (magenta) in Figure 9. We find that the data consistently fall near the diagonal line for a wide range of energies, count rates, and solar wind conditions. Importantly, this consistency of observations and forward model indicate the accuracy of the linear reflection model (equation (5)) over the entire energy range of IBEX-Hi and for all solar wind speeds spanned by the observations.

[44] The derived values of $R_N(E_{SW})$ for each encounter span a wide range, from 0.07 to 0.20. Figure 10 shows that $R_N(E_{SW})$ for hydrogen is strongly ordered by the average solar wind speed. The points were empirically fit over the observed range of solar wind proton energies, yielding

$$R_N(E_{SW}) = \frac{1}{1 + 7.10\,E_{SW}}, \quad (7)$$

where E_{SW}, in units of keV, represents the average over the duration of each encounter. A decrease in $R_N(E_{SW})$ with increasing E_{SW} is consistent with the large body of literature of reflection of H^+ incident on a variety of targets [*Thomas et al.*, 1992; *Eckstein*, 2010], but inconsistent with *Futaana et al.* [2012] who reported no correlation of R_N with solar wind conditions up to v_{SW} = 550 km/s. We furthermore note that the results from the first and third quarter views of the Moon (at opposing azimuthal angles θ) are similar, suggesting a symmetry of the reflection function in azimuthal angle θ.

[45] This analysis has assumed the linear reflection function of equation (5). However, the SRIM simulations, laboratory results of H reflection from C [*Aratari and Eckstein*, 1989], and, as will be discussed, the ENA measurements of *Wieser et al.* [2009], *Rodríguez et al.* [2012], and *Futaana et al.* [2012] all indicate that the reflection function is constant or slowly varying at energies below several hundred electronvolts. For a reflection function that is constant at reflected ENA energies below a threshold energy E_T and linearly decreases at reflected energies greater than E_T, then R_N is reduced by a factor $1 - (E_T/E_{SW})^2$. This is shown as the green dashed line in Figure 9 for E_T = 250 eV, showing a larger reduction in R_N for the slowest solar wind speeds.

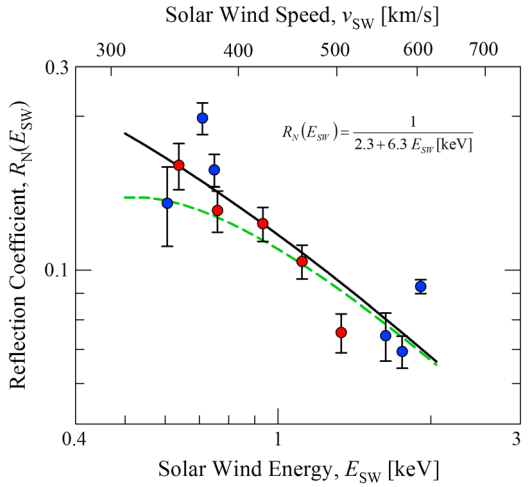

Figure 10. The reflection coefficient of hydrogen ENAs reflected from the Moon exhibits strong dependence on the solar wind speed, with $R_N \approx 0.18$ for slow solar wind and $R_N \approx 0.08$ for fast solar wind. The data are the derived values of R_N depicted in Figure 10. The solid black line is an empirical fit to the data. The green dashed line is the reflection coefficient if the reflection function is a "flat-topped" distribution that is constant below E_T = 250 eV and linearly decreases up to the solar wind energy above E_T = 250 eV. The red and blue points are first and third quarter observations, respectively, and show no difference in R_N. The flat-topped distribution (green dashed line) converges toward the linear distribution (black line) at higher solar wind energies, i.e., for $E_{SW} >> E_T$.

4.3. Comparison with Other Observations of Lunar ENA Emission

[46] In the first reported results of the Chandrayaan-1 Energetic Neutral Atom (CENA) observations, *Wieser et al.* [2009] observed flat energy spectra at low ENA energies up to ~200 eV. Above that energy the ENA energy spectra were observed to fall off steeply, which is in good agreement with the SRIM models presented above (Figure 7, bottom panel) and consistent with the results presented here. Recently, lunar ENAs were also observed with the IBEX-Lo sensor of IBEX [*Rodríguez et al.*, 2012], with a generally flat energy spectrum observed for low energy ENAs and a decrease of the energy spectrum at a fraction of the solar wind energy, also consistent with *Wieser et al.* [2009] and the SRIM results.

[47] *Futaana et al.* [2012] analyzed all available CENA observations in an area near the lunar equator in the energy range from 10 eV to 3.3 keV and empirically derived a Maxwell-Boltzmann (M-B) energy distribution. This distribution is generally flat up to several hundred eV, a result that is consistent with the SRIM results in the bottom panel of Figure 7. Above ~300 eV, the differential ENA flux exponentially decreases.

[48] We can use equation (4) to test the spectral dependence of any reflection function $R(E_{SW}, E, \delta, \theta)$ by comparison with IBEX observations. Figure 11 shows the CENA M-B reflection function from *Futaana et al.* [2012] incorporated into equation (4) and compared to the IBEX data for three cases: slow solar wind (IBEX Orbit 126, $\bar{v}_{SW}$ = 365 km/s, or 0.7 keV), moderate solar wind (IBEX Orbit 101, $\bar{v}_{SW}$ = 465 km/s, or 1.3 keV), and fast solar wind (IBEX Orbit 83, $\bar{v}_{SW}$ = 607 km/s, or 1.9 keV). For all solar wind speeds, the CENA M-B consistently predicts a substantially smaller ENA flux than observed by IBEX at the highest two energy passbands at 1.74 and 2.73 keV. For the moderate solar wind speed observation, the CENA M-B exhibits excellent agreement with the IBEX measurements at the nominal 0.45 keV passband. For the fast solar wind of IBEX Orbit 83, the CENA M-B reflection model shows excellent agreement for measurements at the nominal IBEX-Hi energy passbands 0.45 and 0.71 keV. Therefore, the CENA M-B spectral model systematically under-predicts the ENA flux at the top half of the ENA energy range but accurately predicts portions of the lower half of the energy range if and when it overlaps with the IBEX-Hi energy range. We conclude that the CENA M-B reflection function decreases too rapidly over the top half of the ENA energy distribution, whose maximum corresponds to the energy of the solar wind protons.

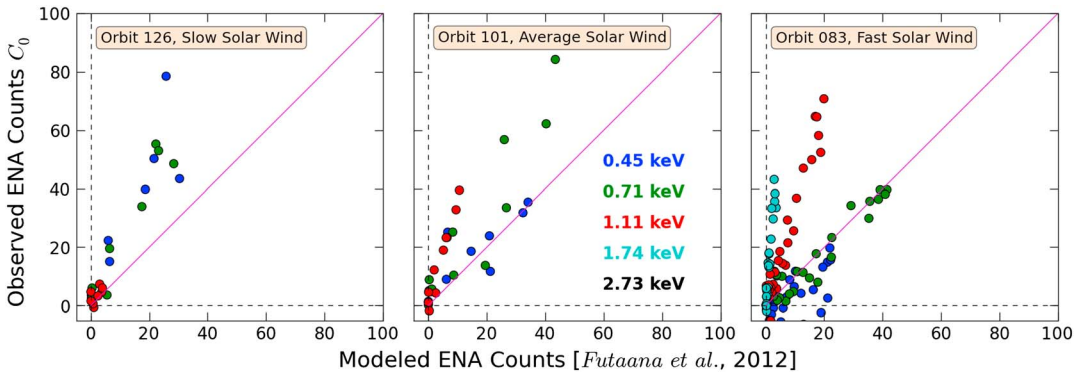

Figure 11. The modeled counts using the reflection function of *Futaana et al.* [2012] Maxwell-Boltzmann (M-B) derived using the Chandrayaan-1 Energetic Neutral Atom (CENA) instrument is compared to IBEX observations of the Moon under slow, moderate, and fast solar wind illumination. The CENA M-B distribution well-predicts the ENA flux observed by IBEX-Hi at lower energies but under-predicts the flux at higher energies.

4.4. Solar Wind Energy Scattered Back to Space: The Energy Reflection Coefficient, R_E

[49] The energy reflection coefficient R_E, which is the fraction of the incoming solar wind energy that is carried by the reflected ENAs is

$$R_E(E_{SW}) = \frac{1}{E_{SW}} \int_{4\pi\ \mathrm{sr}} \int_0^{E_{SW}} E\, R(E_{SW}, E, \delta, \theta) \mathrm{d}E\ \mathrm{d}\Omega\,. \quad (8)$$

[50] Because the scattering processes that underlie reflection result in energy loss by the incoming ion, the energy reflection coefficient will always be less than the reflection coefficient, i.e., $R_E < R_N$. For a reflection function R that decreases linearly with increasing ENA energy up to the solar wind energy (the linear model of equation (5)), the energy reflection coefficient is

$$R_E(E_{SW}) = \frac{1}{3} R_N(E_{SW}). \quad (9)$$

[51] For a reflection function that is flat below an ENA energy E_T (e.g., $E_T \approx 0.25$ keV as used in Figure 10), we obtain

$$R_E(E_{SW}) = \frac{1}{3} R_N(E_{SW}) \left(1 - \left(\frac{E_T}{E_{SW}}\right)^3\right) \quad (10)$$

[52] The term $1-(E_T/E_{SW})^3$ is therefore a correction factor to the linear approximation of equation (9).

[53] Figure 12 shows the average energy per incident solar wind ion that is scattered to space through the reflection process, which is the product $E_{SW}{*}R_E(E_{SW})$, for both the linear model (equation (9)) and flat-topped model (equation (10)). These compare well with the SRIM simulation results using the linear model for R. Because $R_E(E_{SW})$ decreases with increasing solar wind energy, $R_E(E_{SW})$ and E_{SW} partially compensate such that the input energy by the solar wind that is removed by the reflection process varies only 50% over a factor of 4 change in solar wind energy. Additionally, the difference between the linear model and flat-topped models for the reflection function is negligible for fast solar wind and small (<10%) for slow solar wind. For an input power of 5 GW by the solar wind impact the Moon, nearly 0.6 GW of power is radiated to space as ENAs.

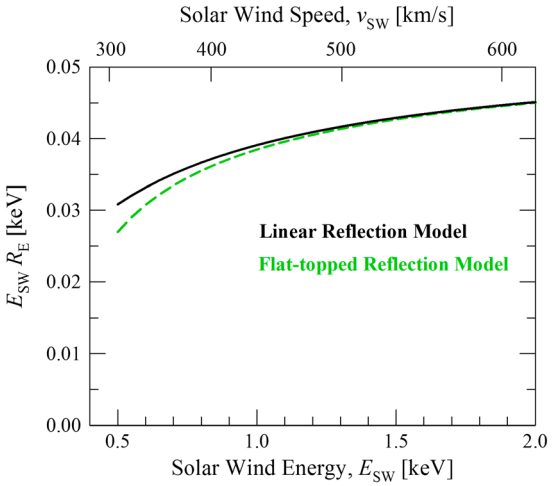

Figure 12. Because R_E is the fraction of the input solar wind energy removed by reflected ENAs, the product $E_{SW}R_E$ is the average energy that is scattered to space by the reflection process that forms ENAs. The two lines represent the linear (equation (9)) and flat-topped (equation (10) with $E_T = 0.25$ keV) spectral models for ENAs emitted from the Moon. The average energy per solar wind ion that impacts the Moon that is carried by ENAs ranges from 0.030 keV for slow solar wind to 0.045 keV for fast solar wind.

4.5. Reflected Energetic Neutral Atoms as Pickup Ions in the Solar Wind

[54] Energetic neutral atoms reflected from a planetary surface follow ballistic trajectories until they are ionized by, for example, photoionization or charge exchange with plasma ions, becoming pickup ions (PUIs) in the solar wind, which is a magnetized plasma. We note that ionization is strongly dependent on radial distance from the Sun [*McComas et al.*, 2012] and is small for ENAs not directed back toward the Sun. An ionized ENA (or equivalently a

proton reflected from the surface as an ion instead of an ENA) experiences a Lorentz force due to the magnetic field in the moving solar wind and gyrates about this field at its initial speed perpendicular to the magnetic field vector in the plasma rest frame. The ensemble of ionized ENAs forms a suprathermal filled-shell flux distribution in velocity space in the solar wind rest frame.

[55] This process is similar to other PUI distributions in the solar wind. For example, interstellar neutrals permeate the heliosphere and are ionized at an initial speed nearly at rest in the heliospheric frame compared to the solar wind speed. In the solar wind reference frame, these PUIs first form a ring distribution in velocity space [*Möbius et al.*, 1985; *Gloeckler et al.*, 1993] that is scattered into a shell distribution and filled through cooling from adiabatic expansion of the solar wind as well as through energy loss processes that heat the core solar wind [e.g., *Gray et al.*, 1996; *Williams et al.*, 1995]. The maximum speed of these PUIs in the solar wind frame is generally v_{SW}.

[56] In contrast, ENAs reflected from a planetary surface (such as the Moon or interplanetary dust) that are subsequently ionized form a filled PUI shell distribution in the solar wind, analogous to a diffuse ENA source [*Bochsler and Möbius*, 2010]. As an example, we consider isotropic ENA emission by an extended source of scattering bodies such as dust, ionized and injected into the solar wind using the simplistic case in which the solar wind magnetic field is perpendicular to the solar wind flow direction. Figure 13 (top) shows the two ENA energy distributions previously considered in Figures 10 and 12, in which the ENA flux linearly decreases with increasing energy (solid black line) and the ENA flux is constant up to 0.5 v_{SW} and linearly decreases with increasing energy (dashed green line) up to v_{SW}. Both are normalized to unity.

[57] The resulting gyrotropic PUI differential flux distributions in the solar wind frame, assuming all ENAs are ionized, are shown in Figure 13 (middle panel). Both the initial linear and flat-topped ENA flux distributions form filled shell PUI distributions that peak between 1 and 1.5 v_{SW}, clearly showing that the ionized ENAs contribute a suprathermal component to the bulk solar wind plasma. An extended source of scattering bodies such as interplanetary dust could generate a small but significant suprathermal population that represents a seed population for acceleration processes in the outer heliosphere. For example, the "outer source" PUI population generated by sputtering from Kuiper belt grains may be a significant contributor to anomalous cosmic rays [*Schwadron and Gloeckler*, 2007]; by comparison, ENA PUIs represent a higher energy suprathermal component and may also contribute to the anomalous cosmic ray distribution.

[58] A representative PUI distribution resulting from ionization of interstellar neutrals (and similar to the distribution of H^+ sputtered from dust) that travel to the inner heliosphere is also shown (red dotted line) in Figure 13 (middle panel). The ISM PUI distribution has been normalized to show the similarity and overlap with the ENA PUI distributions over the range $-1 \le v_{PUI}/v_{SW} \le 1$. We note that the ENA PUI flux distribution lies predominantly at speeds significantly higher than the PUIs from ISM neutral atoms.

[59] Figure 13 (bottom panel) shows the transformation of the PUI flux of Figure 13 (middle panel), into the heliospheric rest frame, analogous to a spacecraft at a fixed radial distance from the Sun and downwind of a source of ionized

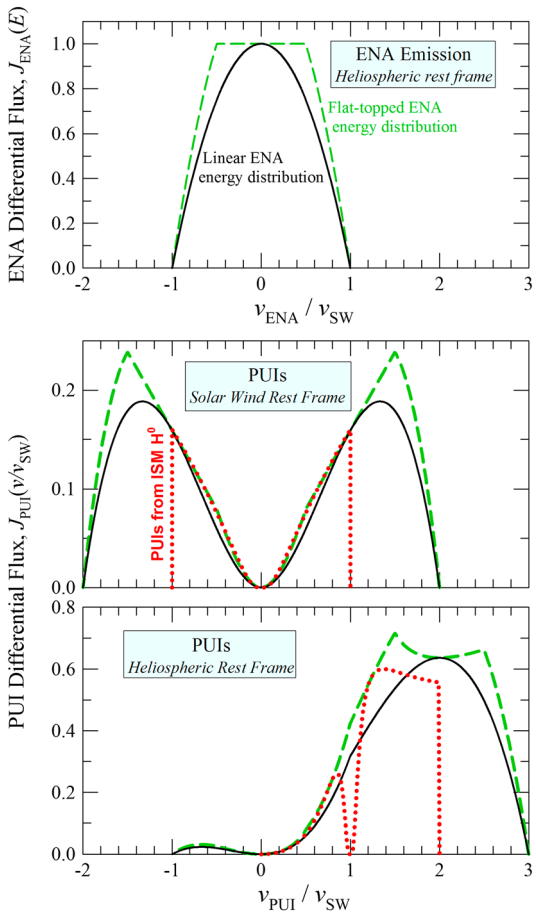

Figure 13. Ionized ENAs from the Moon or interplanetary dust with initial flux distributions (top) are injected gyrotropically into the solar wind, resulting in a filled shell distribution of pickup ions (PUIs) in the rest frame of the solar wind (middle). A negative value of v/v_{SW} corresponds to a direction back toward the Sun. Transforming this PUI distribution into the heliospheric rest frame yields the differential flux (bottom). The dashed green and solid black lines correspond to the linear and flat-topped ENA injection energy distributions used in Figures 10 and 12. The flat-topped distribution for Figure 13 uses a flat ENA emission flux up to $0.5v_{SW}$, which corresponds to E_T = 0.25 keV and E_{SW} = 1 keV. As explained in Figure 10, the linear approximation applies when v_{SW} equals or exceeds the fast solar wind speed. The PUI flux in the bottom panel is characteristic of what might be observed downstream of an extended scattering source such as interplanetary dust due to reflected solar wind protons. The red dotted line corresponds to the characteristic flux distribution resulting from ionization of cold interstellar neutral atoms that travel to the inner heliosphere.

ENAs. The corresponding PUI distribution from ISM neutrals is normalized to show that it generally follows the same dependence on v_{PUI}/v_{SW} as the ENA PUI distribution over the range $0 \le v_{PUI}/v_{SW} \le 2$. However, most ENA PUIs will be observed at speeds greater than $1.5v_{SW}$ and up to $3v_{SW}$, substantially beyond the maximum speed of the PUI distribution from ISM neutral atoms. Thus, ionized ENAs reflected from the planetary surfaces result in a PUI distribution with maximum speed $3v_{sw}$ in the solar rest frame as

shown in Figure 13 (bottom panel). While the fraction of ionized ENAs from this process is likely to be small due to sparsity of interplanetary dust and the low probability of subsequent ENA ionization, this demonstrates a unique signature of PUIs resulting from the ENA reflection process associated with plasmas that flow past solid objects.

5. Beyond the Moon

[60] These lunar results apply to any airless solid object exposed to a plasma environment. In our solar system, this includes the moons of other planets, Mercury, asteroids, comets, interplanetary dust, and dust streams of Jupiter and Saturn [e.g., *Hsu et al*., 2011]. Beyond our solar system, dust, which is ~1% of the baryonic mass of our galaxy, is an essential component for protoplanetary disks [*Beckwith et al*., 2000] and stellar formation [*D'Alessio et al*., 2006] and is redistributed into the interstellar medium at late stages of asymptotic giant branch stars [*Ferrarotti and Gail*, 2006] or through supernovae [*Dunne et al*., 2003; *Bianchi and Schneider*, 2007]. All of these involve coupled interactions of dust and plasma.

[61] We can distinguish the dust-plasma interactions for two cases based on the relative bulk velocity $\overrightarrow{v_b}$ between the dust and a magnetized plasma relative to the thermal ion speed, v_{th}. First, we consider the case in which the bulk plasma and dust reside in the same reference frame, i.e., $v_b << v_{th}$. Dust grains embedded in a hot gas have been recognized as an efficient cooling mechanism in which charged particle energy is converted to thermal energy in the grain and subsequently emitted in the infrared [*Ostriker and Silk*, 1973; *Burke and Silk*, 1974]. This process, which can have significant impact on the dynamics of astrophysical processes such as shocks [*Silk and Burke*, 1974; *Draine*, 1981], applies equally to reflection, capturing much of an ion's kinetic energy (e.g., Figure 12). Additionally, because most ions are reflected as neutrals, the reflection and implantation processes both act as a sink for the ion's potential energy by providing an efficient pathway for neutralization. With ionization potentials of 13.6 eV for H^+ and 24.6 eV for He^+, the potential energy sink alone may be a dominant process for plasmas up to ~10^5 K.

[62] The second case, in which $v_b >> v_{th}$, is analogous to the Moon immersed in the magnetized solar wind flow, for which the results of Figure 13 can be generally applied, substituting v_b for v_{SW}. The flat-topped and linear ENA flux distributions converge when v_b equals or exceeds the fast solar wind speed as discussed in Figure 10. For this case of a scattering object immersed in a fast flowing magnetized plasma, the resulting reflected ENAs and ions represent a potentially strong suprathermal component to the core plasma. The ionized suprathermal ENAs heat the plasma over astronomical scales and represent seed particles for acceleration processes similar to those that lead to anomalous cosmic ray formation from PUIs in our heliosphere [e.g., *Jokipii*, 1987].

[63] **Acknowledgments.** We gratefully acknowledge all of the contributions made by the entire IBEX team who have been and are making this mission a tremendous success. IBEX and this work were funded by NASA as a part of the Explorer Program. Work at Los Alamos was performed under the auspices of the US Department of Energy. Work by E. Möbius on PUIs was supported under SR&T Grant NNX09AW32G.

References

Aratari, R., and W. Eckstein (1989), Reflection of hydrogen from carbon, *J. Nucl. Mat.*, *162*, 910–914, doi:10.1016/0022-3115(89)90384-X.

Bandurko, V. V., N. N. Koborov, V. A. Kurnaev, V. M. Sotnikov, and O. V. Zabeyda (1990), Low energy hydrogen and helium ions backscattering from surfaces with structure, *J. Nucl. Mat.*, *176–177*, 630–634, doi:10.1016/0022-3115(90)90118-7.

Barabash, S., et al. (2009), Investigation of the solar wind-Moon interaction onboard Chandrayaan-1 mission with the SARA experiment, *Curr. Sci. India*, *96(4)*, 526–532.

Beckwith, S. V. W., T. Henning, and Y. Nakagawa (2000), Dust Properties and Assembly of Large Particles in Protoplanetary Disks, in *Protostars and Planets IV*, ed. V. Mannings, A. P. Boss, S. S. Russell, Tucson: Univ. Arizona Press, 533.

Bianchi, S., and Schneider, R. (2007), Dust formation and survival in supernova ejecta. *Mon. Not. R. Astron. Soc.*, *378*, 973–982, doi:10.1111/j.1365-2966.2007.11829.x.

Bochsler, P., and E. Möbius (2010), Energetic Neutral Atoms: An Additional Source for Heliospheric Pickup Ions, *Astrophys. J. Lett.*, *721*, L6, 10.1088/2041-8205/721/1/L6.

Buratti, B. J., J. K. Hillier, M. Wang (1996), The Lunar Opposition Surge: Observations by Clementine, *Icarus*, *124*, 490–499, doi:10.1006/icar.1996.0225.

Burke, J. R., and J. Silk (1974), Dust grains in a hot gas. I. Basic Physics, *Astrophys. J.*, *190*, 1–10, doi:10.1086/152840.

Carrier, W. (2003), Particle Size Distribution of Lunar Soil, *J. Geotech. Geoenviron. Eng.*, *129*(10), 956–959, doi:10.1061/(ASCE)1090-0241(2003)129:10(956).

Cassidy, T. A., and R. E. Johnson (2005), Monte Carlo model of sputtering and other ejection processes within a regolith, *Icarus*, *176*, 499–507, doi:10.1016/j.icarus.2005.02.013.

D'Alessio, P., N. Calvet, L. Hartmann, R. Franco-Hernandez, and H. Servin (2006), Effects of dust growth and settling in T Tauri disks, *Astrophys. J.*, *638*, 314–335, doi:10.1086/498861.

Draine, B. T. (1981), Infrared emission from dust in shocked gas, *Astrophys. J.*, *245*, 880–890, doi:10.1086/158864.

Dunne, L., S. Eales, R. Ivison, H. Morgan, and M. G. Edmunds (2003), Type II supernovae as a significant source of interstellar dust, *Nature 424*, 285–287, doi:10.1038/nature01792.

Eckstein, W. (1997), Physical sputtering and reflection processes in plasma-wall interactions, *J. Nucl. Mat.*, *248*, 1–8, doi:10.1016/S0022-3115(97)00109-8.

Eckstein, W. (2010), Reflection (Backscattering), *B. Russ. Acad. Sci.-Physics*, *74*, 141–148.

Elphic, R. C., H. O. Funsten, B. L. Barraclough, D. J. McComas, M. T. Paffett, D. T. Vaniman, and G. Heiken (1991), Lunar surface composition and solar wind-induced secondary ion mass spectrometry, *Geophys. Res. Lett.*, *18*, 2165–2168, doi:10.1029/91GL02669.

Feldman, W. C., J. T. Gosling, D. J. McComas, and J. L. Phillips (1993), Evidence for ion jets in the high-speed solar wind, *J. Geophys. Res.*, *98*, 5593–5605, doi:10.1029/92JA02260.

Ferrarotti, A. S., and H.-P. Gail (2006), Composition and quantities of dust produced by AGB-stars and returned to the interstellar medium, *Astron. Astrophys.*, *447*, 553–576, doi:10.1051/0004-6361:20041198.

Funsten, H. O., et al. (2009a), The Interstellar Boundary Explorer High Energy (IBEX-Hi) Neutral Atom Imager, *Space Sci. Rev.*, *146*, 75–103, doi:10.1007/s11214-009-9504-y.

Funsten, H. O., et al (2009b), Structures and Spectral Variations of the Outer Heliosphere in the IBEX Energetic Neutral Atom Sky Maps, *Science*, *326*, 964-966, doi:10.1126/science.1180927.

Fuselier, S. A., et al. (2009), The IBEX-Lo Sensor, *Space Sci. Rev.*, *146*, 117–147, doi:10.1007/s11214-009-9495-8.

Futaana, Y., S. Barabash, M. Wieser, M. Holmstrom, C. Lue, P. Wurz, A. Schaufelberger, A. Bhardwaj, M. B. Dhanya, and K. Asamura (2012), Empirical energy spectra of neutralized solar wind protons from the lunar regolith, *J. Geophys. Res.- Planets*, *117*, E05005, doi:10.1029/2011JE004019.

Gloeckler, G., A. B. Galvin, F. M. Ipavich, J. Geiss, H. Balsiger, R. von Steiger, L. A. Fisk, K. W. Ogilvie, and B. Wilken (1993), Detection of Interstellar Pick-Up Hydrogen in the Solar System, *Science*, *261*, 70–73, doi:10.1126/science.261.5117.70.

Gray, P. C., C. W. Smith, W. H. Matthaeus, and N. F. Otani (1996), Heating of the solar wind by pickup ion driven Alfvén ion cyclotron instability, *Geophys. Res. Lett.*, *23(2)*, 113–116, doi:10.1029/95GL03707.

Hammond, C. M., W. C. Feldman, J. L. Phillips, B. E. Goldstein, and A. Balogh (1995), Solar wind double ion beams and the heliospheric current sheet, *J. Geophys. Res.*, *100*, 7881–7889, doi:10.1029/94JA03304.

Haskin, L. A., and P. Warren (1991), Lunar Chemistry, in *Lunar Sourcebook*, edited by G. H. Heiken, D. T. Vaniman, and B. M. French, pp. 357–474, Cambridge Univ. Press, New York.

Hapke, B. (1986), On the sputter alteration of regoliths of outer solar system bodies, *Icarus*, *66*, 270–279, doi:10.1016/0019-1035(86)90157-0.

Hsu, H.-W., S. Kempf, F. Postberg, M. Trieloff, M. Burton, M. Roy, G. Moragas-Klostermeyer, and R. Srama (2011), Cassini dust stream particle measurements during the first three orbits at Saturn, *J. Geophys. Res.*, *116*, A08213, doi:10.1029/2010JA015959.

Houston, W. N., J. K. Mitchell, and W. D. Carrier (1974), Lunar soil density and porosity, *Proc. 5th Lunar Sci. Conf., Geochim. Cosmochim. Acta (Suppl. 5)*, *3*, 2361–2364.

Johnson, R. E., and R. Baragiola (1991), Lunar surface – sputtering and secondary ion mass spectrometry, *Geophys. Res. Lett. 18*, 2169–2172, doi:10.1029/91GL02095.

Jokipii, J. R. (1987), Rate of energy gain and maximum energy in diffusive shock acceleration, *Astrophys. J.*, *313*, 842–846, doi:10.1086/165022.

Keller, L. P., and D. S. McKay (1993), Discovery of vapor deposits in the lunar regolith, *Science*, *261*, 1305–1307, doi:10.1126/science.261.5126.1305.

Lawrence, D. J., W. C. Feldman, R. C. Elphic, R. C. Little, T. H. Prettyman, S. Maurice, P. G. Lucey, and A. B. Binder (2002), Iron abundances on the lunar surface as measured by the Lunar Prospector gamma-ray and neutron spectrometers, *J. Geophys. Res.-Planets*, *107*, 5130, doi:10.1029/2001JE001530.

Lucey P. (2006), Understanding the lunar surface and space-Moon interaction, *New Views of the Moon, Rev. Min. Geochem. 60*, 82–219, doi: 10.2138/rmg.2006.60.2.

Mayer, M., W. Eckstein, and B. M. U. Scherzer (1995), Reflection of low energy hydrogen from carbon at oblique incidence, *J. Appl. Phys.*, *77*, 6609–6615, doi:10.1063/1.359071.

McComas, D. J., S. J. Bame, P. Barker, W. C. Feldman, J. L. Phillips, P. Riley, and J. W. Griffee (1998), Solar wind electron proton alpha monitor (SWEPAM) for the advanced composition explorer, *Space Sci. Rev.*, *86*, 563–612, doi:10.1023/A:1005040232597.

McComas, D. J., F. Allegrini, P. Bochsler, P. Frisch, H. O. Funsten, M. Gruntman, P. H. Janzen, H. Kucharek, E. Moebius, D. B. Reisenfeld, and N. A. Schwadron (2009a), Lunar Backscatter and Neutralization of Solar Wind Ions: First Neutral Atom Observations of the Moon, *Geophys. Res. Lett.*, *36*, L12104, doi:10.1029/2009GL038794.

McComas, D. J. (2009b), IBEX - Interstellar Boundary Explorer, *Space Sci. Rev.*, *146*, 11–33, doi:10.1007/s11214-009-9499-4.

McComas, D. J. (2009c), First Global Observations of the Interstellar Interaction from the Interstellar Boundary Explorer, *Science*, *326*, 959–962, doi:10.1126/science.1180906.

McComas, D. J. (2011), A new class of long-term stable lunar resonance orbits: Space weather applications and the Interstellar Boundary Explorer, *Space Weather*, *9*, S11002, doi:10.1029/2011SW000704.

McComas, D. J. (2012), The first three years of IBEX observations and our evolving heliosphere, *Astrophys. J. Suppl. Ser.*, *203*:1, doi:10.1088/0067-0049/203/1/1.

McKay, D. S., G. Heiken, A. Basu, G. Blanford, S. Simon, R. Reedy, B. M. French, and J. Papike (1991), The lunar regolith, in *Lunar Sourcebook*, edited by G. H. Heiken, D. T. Vaniman, and B. M French, p. 285–356, Cambridge Univ. Press, New York.

Möbius, E., D. Hovestadt, B. Klecker, M. Scholer, G. Gloeckler, and F. M. Ipavich (1985), Direct observation of He+ pick-up ions of interstellar origin in the solar wind, *Nature*, *318*, 426–429, doi:10.1038/318426a0.

Ogilvie, K. W. (1995), SWE, A comprehensive plasma instrument for the Wind spacecraft, *Space Sci. Rev.*, *71*, 55–77, doi:10.1007/BF00751326.

Ostriker, J. P., and J. Silk (1973), Dust cooling of hot gas, *Astrophys. J.*, *184*, L113–L115, doi:10.1086/181301.

Pillinger, C. T. (1979), Solar-wind exposure effects in the lunar soil, *Rep. Prog. Phys.*, *42*, 897–962, doi:10.1088/0034-4885/42/5/003.

Rodríguez D. F., L. Saul, P. Wurz, S. A. Fuselier, H. O. Funsten, D. J. McComas, and E. Möbius (2012), IBEX-Lo Observations of Energetic Neutral Hydrogen Atoms Originating from the Lunar Surface, *Planet. Space Sci.*, *60*, 297–303, doi:10.1016/j.pss.2011.09.009.

Rosenburg, M. A., O. Aharonson, J. W. Head, M. A. Kreslavsky, E. Mazarico, G. A. Neumann, D. E. Smith, M. H. Torrence, and M. T. Zuber (2011), Global surface slopes and roughness of the Moon from the Lunar Orbiter Laser Altimeter, *J. Geophys. Res.*, *116*, E02001, doi:10.1029/2010JE003716.

Saito, Y. (2008), Solar wind proton reflection at the lunar surface: Low energy ion measurement by MAP-PACE onboard SELENE (KAGUYA), *Geophys. Res. Lett.*, *35*, L24205, doi:10.1029/2008GL036077.

Schaufelberger, A., P. Wurz, S. Barabash, M. Wieser, Y. Futaana, M. Holmström, A. Bhardwaj, M. B. Dhanya, R. Sridharan, and K. Asamura (2011), Scattering function for energetic neutral hydrogen atoms off the lunar surface, *Geophys. Res. Lett.*, *38*, L22202, doi:10.1029/2011GL049362.

Schwadron, N. A. (2009), Comparison of Interstellar Boundary Explorer Observations with 3-D Global Heliospheric Models, *Science*, *326*, 966–968, doi:10.1126/science.1180986.

Schwadron, N. A., and G. Gloeckler (2007), Pickup ions and cosmic rays from dust in the heliosphere, *Space Sci. Rev.*, *130*, 283–291, doi:10.1007/s11214-007-9166-6.

Shkuratov, Y., V. Kaydash, V. Korokhin, Y. Velikodsky, N. Opanasenko, and G. Videen (2011), Optical measurements of the Moon as a tool to study its surface, *Planet. Space Sci.*, *59*, 1326–1371, doi:10.1016/j.pss.2011.06.011.

Sigmund, P. (1982), Kinetic theory of particle stopping in a medium with internal motion, *Phys. Rev. A*, *26*, 2497–2517, doi:10.1103/PhysRevA.26.2497.

Silk, J., and J. R. Burke (1974), Dust grains in a hot gas. II. Astrophysical applications, *Astrophys. J.*, *190*, 11–17, doi:10.1086/152841.

Thomas, E. W., R. K. Janev, and J. J. Smith (1992), Scaling of particle reflection coefficients, *Nucl. Instrum. Meth. B*, *69*, 427–436, doi:10.1016/0168-583X(92)95298-6.

Vicanek, M., and H. M. Urbassek (1991), Reflection coefficient of low-energy light ions, *Phys. Rev. B*, *44*, 7234–7242, doi:10.1103/PhysRevB.44.7234.

Wehner, G. K., C. Kenknight, and D. L. Rosenberg (1963), Sputtering rates under solar wind bombardment, *Planet. Space Sci.*, *11*, 885–895, doi:10.1016/0032-0633(63)90120-X.

Wieser, M., S. Barabash, Y. Futaana, M. Holmstrom, A. Bhardwaj, R. Sridharan, M. B. Dhanya, P. Wurz, A. Schaufelberger, and K. Asamura (2009), Extremely high reflection of solar wind protons as neutral hydrogen atoms from regolith in space, *Planet. Space Sci.*, *57*, 2132–2134, doi:10.1016/j.pss.2009.09.012.

Williams, L. L., G. P. Zank, and W. H. Matthaeus (1995), Dissipation of pickup-induced waves: A solar wind temperature increase in the outer heliosphere? *J. Geophys. Res.*, *100(*A9*)*, 17,059–17,067, doi:10.1029/95JA01261.

Wurz, P. (2009), IBEX Backgrounds and Signal to Noise Ratio, *Space Sci. Rev.*, *146*, 173–206, doi:10.1007/s11214-009-9515-8.

Ziegler, J. F., M. D. Ziegler, J. P. Biersack (2010), The stopping and range of ions in matter, *Nucl. Instum. Meth. B*, *268*, 1818–1823, doi:10.1016/j.nimb.2010.02.091.